

# GNSS Multipath Error Modeling for Automotive Applications

Samer Khanafseh, Birendra Kujur *Illinois Institute of Technology*,  
Mathieu Joerger, *The University of Arizona*,  
Todd Walter, Sam Pullen, Juan Blanch, *Stanford University*,  
Kevin Doherty, Laura Norman, Lance de Groot, *Hexagon Positioning Intelligence*,  
Boris Pervan, *Illinois Institute of Technology*

## ABSTRACT

In this paper, we provide GNSS multipath error models for automotive applications by leveraging methods used in aviation applications. These error models are intended for navigation integrity and continuity risk evaluation. We provide error models for code and carrier phase GNSS measurements under both static and dynamic multipath environments. The dynamic dataset was collected in realistic driving conditions for a vehicle traveling in an urban canyon and on a highway with overpasses and road signs. The static test was conducted in a more controlled environment, first, to precisely evaluate measurement errors under open sky, and then, to quantify the effect on multipath error of a semi-truck next to a car equipped with a commercial GNSS antenna. In this paper, we characterize the errors by the mean and standard deviation of a bounding Gaussian distribution and by the autocorrelation time constant of the measurement errors.

## INTRODUCTION

There has recently been an increased interest from automated vehicle manufacturers in using GNSS as a complement to other sensors including vision, lidar, radar, etc. In order to achieve full autonomy, the navigation system must have high levels of integrity and continuity. High-integrity navigation systems such as the Wide and Local Area Augmentation Systems (WAAS and LAAS, respectively) exist, but are designed for aviation applications and may not provide sufficient accuracy for automated ground vehicle applications. In this work, we use techniques of safety-critical aviation navigation to provide error models for GNSS signals in automotive applications.

Evaluating integrity and continuity requires that the positioning error distribution be determined. To do so, the first step is to derive fault-free (or nominal) error models of the measurements. Typically, the actual error distributions from different satellites are convolved in linear (or linearized) estimators and produce a position error distribution. For linear (or linearized) estimators, DeCleene showed that if the cumulative distribution function (CDF) of the actual measurement errors could be overbounded, then the actual estimate error CDF would be overbounded by that of the convolution of the bounding measurement error CDFs [1]. This approach remained valid assuming that the measurement error CDFs were zero-mean, unimodal, and symmetric. Rife built upon this work to establish the paired-overbounding method, which no longer requires that these limiting assumptions be true [2]. In this paper, we use the paired Gaussian over-bounding method to derive GNSS measurement error models [2]. An empirical CDF is obtained from experimental data under a given test scenario, and is used to determine the mean and standard deviation of the Gaussian over-bounding CDF, which defines the error model.

In order to study the multipath effects on L1 and L2 pseudorange (code) measurements individually, iono-corrected code minus carrier (CMC) observations are used. Ionospheric delay is estimated and removed using L1 and L2 carrier phase measurements. CMC observables are mainly dominated by the code multipath and code thermal noise errors, and therefore, will be used to derive pseudorange receiver noise and multipath error models. This type of error evaluation was carried out before for aircraft applications [5-8], and for specific ground applications (e.g., including [9-10]). In this paper, we carry out new multipath error analyses for car applications in both static and dynamic conditions.

In addition, in order to quantify the multipath effect on carrier phase measurements, we compute the double differenced carrier phase residuals considering pairs of satellite signals, and a pair of antennas located in the same vicinity. Due to the sensitivity of double differenced carrier phase residuals to baseline vector accuracy, this analysis is conducted for static

antennas only. In order to isolate the source of the multipath error to the antenna of interest, we place the reference antenna at a location where it is not affected by multipath reflections. To isolate a satellite of interest, we pick one of the satellites in the pair to be a high elevation reference satellite (above 33 deg) unlikely to be significantly affected by multipath errors.

Autocorrelation functions of CMC are also computed to provide a temporal model of the errors. When the integrity risk of a Kalman filter-based positioning solution is required, it is important to capture the temporal characteristics of the measurement noise. Multipath can be modeled as a first order Gauss Markov process, with a time constant to be determined from experimental data. This analysis will provide an empirical justification for the value of the time constant. Recent work in [3] describes a method to overbound the integrity risk given lower and upper bounds on the time constants of the colored noise's autocorrelation function.

Thus, in this paper, we present a methodology to quantify pseudorange and carrier phase measurement errors in postprocessing. We also provide preliminary error models for code and carrier phase measurement noise and multipath errors in controlled conditions and in realistic automotive environments. These results can then be used in evaluating different navigation systems ability to meet specific integrity, continuity and availability requirements.

### STATIC TEST

Experimental data for an example GNSS receiver and antenna was collected to establish error models. The first part of the static test was carried out in clear-sky conditions without signal reflectors. Since this study is tailored toward autonomous applications, the antennas were not equipped with any hardware to limit ground multipath (like choke rings, for example). Once the error model characteristics were captured for clear sky environments, we wanted to capture the effect on ranging errors of reflectors around a car's GNSS antenna. For a car driving in autonomous mode, there can be many reflectors altering signal reception, for example when the car drives next to a truck. In the case of slow relative motion between the car and truck (e.g. in heavy traffic), the truck might cause persistent signal reflections at the antenna. In order to evaluate the effect of such a scenario on GNSS errors, a controlled experiment was devised.

In this experiment, a pair of NovAtel (a part of Hexagon Positioning Intelligence) antennas were used: a NovAtel prototype automotive grade dual frequency antenna GNSS1500, and NovAtel geodesy grade 702-GGL. The antennas were fixed on tripods placed at about 2.2m baseline and 3.7 m away from a truck. An additional 702-GGL antenna was located far away from the truck, on the rooftop of a nearby building. Three 24-hour GNSS datasets were collected. Each set is collected at 30 second update interval. The first dataset was collected in absence of the truck to capture a clear-sky scenario; in the second set (referred to as E-W) the truck was oriented in the East-West direction at about 3.7m to the north of the antenna pair; and in the third set (referred to as N-S) the truck was rotated to face North-South and was placed at about the same distance west of the antennas (Figure 1). Although the data was collected using two different receivers (NovAtel OEM-Flex6 and NovAtel WAAS G-III), only OEM-Flex6 data is analyzed in this paper.

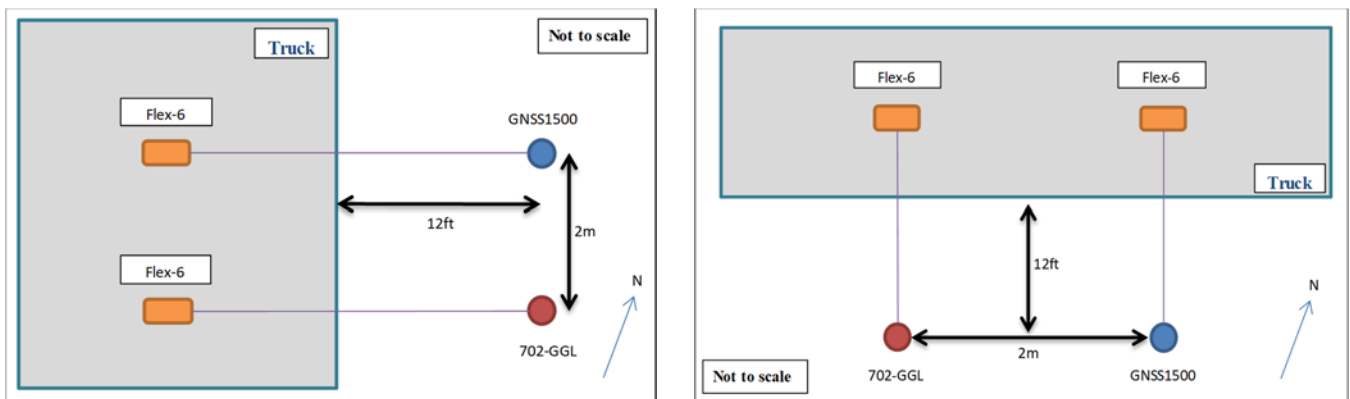


Figure 1: Static test configurations as described in [1]

We are interested in evaluating signal tracking errors at both the L1 and L2 frequencies individually. Thus, instead of using iono-free code-minus-carrier, we consider iono-corrected code-minus-carrier data. When processing the data, biased ionospheric delay  $I$  is first estimated using the L1 and L2 carrier phase measurements  $\phi$  as shown in (1) [4],

$$\hat{I}_{L1} = \frac{f_{L2}^2}{f_{L1}^2 - f_{L2}^2} (\phi_{L1} - \phi_{L2}) = I_{L1} + \lambda_{L1} n_{L1} - \lambda_{L2} n_{L2} + \frac{f_{L2}^2}{f_{L1}^2 - f_{L2}^2} (v_{\phi L1} - v_{\phi L2}) \quad (1)$$

where  $\hat{I}$  is the estimated ionospheric delay at the L1 or L2 frequency,  $f_{L1/L2}$  is the L1/L2 frequency,  $\lambda_{L1/L2}$  is the L1/L2 wavelength,  $n_{L1/L2}$  is the L1/L2 carrier phase cycle ambiguity bias, and  $v$  is the carrier phase measurement noise including multipath and thermal noise. The estimated ionospheric delay in (1) is then used to compensate for the ionospheric effects from the difference between code and carrier phase measurements (2) and (3).

$$z'_{CMCL1} = \rho_{L1} - \phi_{L1} = 2I_{L1} - \lambda_{L1} n_{L1} + v_{\rho L1} - v_{\phi L1} \quad (2)$$

$$z_{CMCL1} = z'_{CMCL1} - 2\hat{I}_{L1} = 2\lambda_{L2} n_{L2} - 3\lambda_{L1} n_{L1} + v_{\rho L1} - \left( v_{\phi L1} + 2 \frac{f_{L2}^2}{f_{L1}^2 - f_{L2}^2} (v_{\phi L1} - v_{\phi L2}) \right) \quad (3)$$

where  $z_{CMC}$  is the code-minus-carrier observable and  $\rho$  is the pseudorange. Because the result of this computation is biased by  $(2\lambda_{L2} n_{L2} - 3\lambda_{L1} n_{L1})$ , we remove the mean value from the data set, which results in iono-corrected code-minus-carrier observables (CMC). As (3) shows, CMC observables are mainly dominated by the code multipath and code thermal noise errors. The same computation in (3) can be performed for the L2 frequency, considering that the L2 ionospheric delay can be obtained using

$$\hat{I}_{L2} = \frac{f_{L1}^2}{f_{L2}^2} \hat{I}_{L1} \quad (4)$$

Figure 2 shows the computed GPS CMC for the three days of data: No truck, E-W truck, and N-S truck cases.

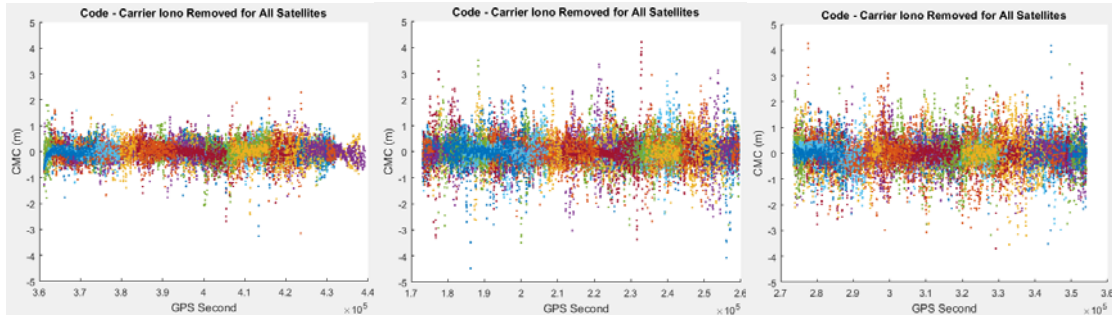


Figure 2: CMC for the three sets of data. From left to right: No Truck set, E-W set, and N-S set.

Comparing CMC of the No Truck set to E-W or N-S clearly demonstrates the multipath error effect resulting from the semi-truck next to the antennas: the magnitude of both the nominal errors and of the outliers are much larger in the E-W and NS sets than in the No Truck set. Since multipath is related to how the antenna is located with respect to the surrounding reflectors (the truck in this case), the CMC values are represented in Figure 3 and Figure 4 on polar azimuth-elevation plots with color maps corresponding to the error magnitude. The color maps are calibrated such that the white color indicates 0 error, navy blue is -5m error and red is +5m error. The darker (or more pronounced) the color appears, the larger the corresponding CMC error is. By comparing the No-truck set to the E-W set, Figure 3 shows that larger errors are observed in the E-W set for the southern satellite tracks (circled in red) with few more in the northern tracks. The errors in the northern side can be justified by additional errors due to weaker signals that penetrated the truck canopy. The southern region is the one that is caused by multipath due to the signal bouncing off the truck trailer. Similar behavior is observed for the N-S data (Figure 4), where the multipath data is concentrated in the eastern side of the plot and signal penetration are on the western side.

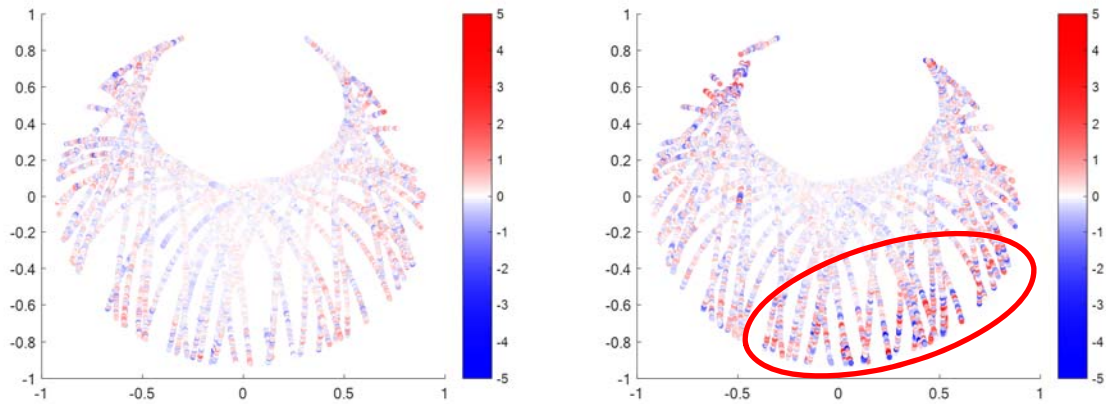


Figure 3: CMC error values projected on sky-plot azimuth elevation satellite tracks. Left: No Truck set, Right: E-W set.

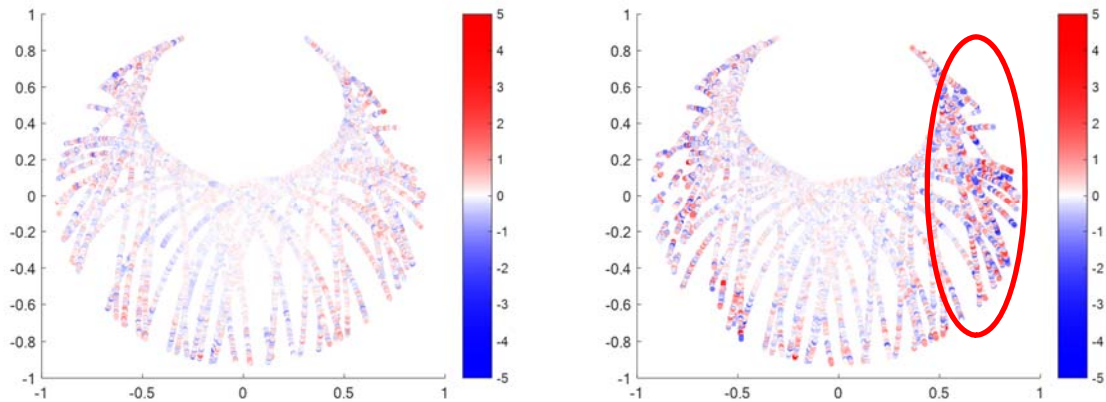


Figure 4: CMC error values projected on sky-plot azimuth elevation satellite tracks. Left: No Truck set, Right: N-S set.

If multipath regions due to the truck are isolated, then the error models for the truck multipath can be evaluated. Since this was a controlled experiment with known truck and antenna geometry, we decided to use the truck geometry to isolate several multipath regions. Figure 5 shows schematics of a U-Haul 15' truck that was used in the experiment, with the estimated antenna height and placement. The azimuth and elevation (Az-El) regions where the signal will penetrate the truck and where multipath reflection is expected to occur were computed geometrically and are highlighted in the figure. When these computed Az-El regions were overlaid on top of the CMC errors in Figure 4, they approximately matched the large CMC errors (Figure 6). The penetration and MP regions for the 702 and 1500 antennas in N-S and E-W sets are shown in Table 1.

Table 1: Az-El range for the penetration and multipath regions

Data set	Ant.	Region	EL range (deg)	AZ range (deg)
N-S	1500	Penetration	0-33	219.1-304.4
		Multipath		55.6-140.9
	702	Penetration		235.6-320.9
		Multipath		39.1-124.4
E-W	1500	Penetration		309.1-34.4
		Multipath		145.6-230.9
	702	Penetration		325.6-50.9
		Multipath		129.1-214.4

In this report, we use the folded cumulative distribution function (folded-CDF) bounding method to evaluate the error models [1] and [2]. In the folded CDF representation, the empirical CDF is computed for the data and then compared to a Gaussian CDF with bounding mean and bounding standard deviation to be determined. Folded in this context means that the left tail likelihood is computed for error magnitudes lower than the data set's median value, and the right tail likelihood is computed for error magnitudes larger than the median value. Gaussian CDFs with mean and standard deviation values that overbound all points of the empirical CDF are referred to as bounding Gaussian distributions, and will be used for error modeling. When providing the error models in the following sections, and whenever applicable, we categorize the results in four sets:

- 1- Aggregate: for all data points,
- 2- Penetration region: where the satellite signal penetrates the truck,
- 3- Multipath (MP) region: for signals in the MP overlaid region,
- 4- No-MP region: for signals outside the MP and penetration regions.

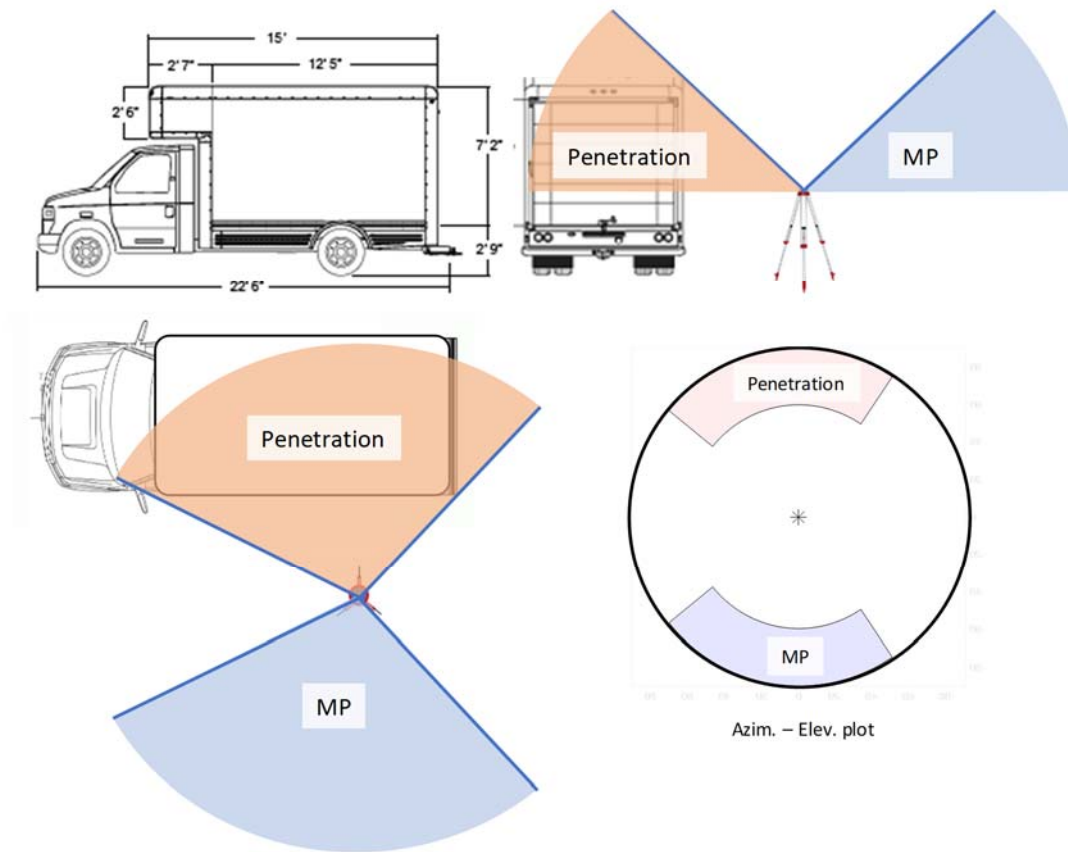


Figure 5: U-Haul truck schematic with penetration and multipath Az-El regions highlighted

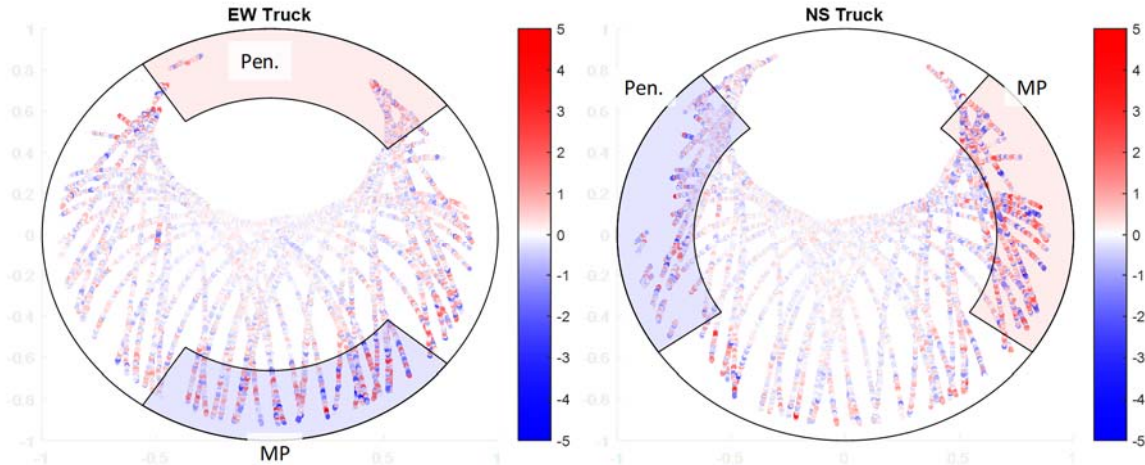


Figure 6: CMC error values projected on sky-plot azimuth elevation satellite tracks with the penetration and multipath regions overlaid on top. Left: E-W Truck set, Right: N-S set.

A. Bounding standard deviation results – Pseudorange

For the static analysis, time segments shorter than 600sec were removed. Figure 7 shows the CDF bounding plot for the No-Truck GPS case. The empirical CDF from the CMC data is shown in blue. A Gaussian CDF is shown in cyan with mean of 0.6 cm and standard deviation of 32.4 cm (corresponding to the data set sample mean and sample standard deviation). The bounding Gaussian CDF is shown in red. In this case, the data is CDF-bounded by a Gaussian with a mean of 0.6 cm and standard deviation of 84.3 cm. These bounding values are the ones that should be used in the navigation estimator and in protection levels (PL) computation. It is worth noting that in this analysis, no distinction is done between thermal noise and multipath, and the resultant standard deviation represents the combined effect. This point can be refined in future analysis.

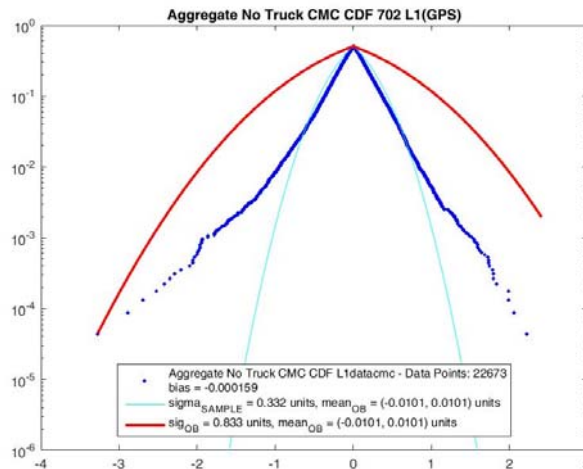


Figure 7: CMC error CDF bounding curve for the No-Truck case

The same bounding process is then repeated for the E-W and N-S data for all antennas and frequencies. A summary of the results for both GPS and GLONASS is given in Tables 2 – 3. In general, the results illustrate that penetration and MP regions have non-zero mean and that the bounding standard deviation for these regions is larger than the nominal clear sky conditions. The results also show that in general L2 multipath errors are larger than for L1, and that multipath error standard deviations of the 1500 antenna is slightly worse than for the 702 antenna.

The results also indicate that a worst-case code standard deviation of 2 m for GPS and 1.85 m for GLONASS can be used in the estimator to compute the PL, with a mean of 17 cm. If, with these extreme error model parameter values, the navigation

system meets the requirements (to be specified for autonomous car navigation, as for example in [11]), then the no further analysis and modeling is needed to distinguish between multipath or penetration regions. If, on the other hand, the requirements are not met, a more elaborate model can be used with different parameter values based on elevation, for example. It is noteworthy that bounding sigma values for the low elevation region ( $< 33^\circ$ ) are smaller than for the multipath regions. This is because the bound for the low elevation region includes regions not affected by the truck-induced multipath errors (Figure 6), which may have smaller errors. In contrast, the high-elevation region's bounding sigma can have lower values as compared with the region after multipath and penetration regions are excluded, because the latter may include large errors at lower elevations. The system may safely use high elevation values for satellites higher than  $33^\circ$  elevation angles, and use the multipath bounding values for lower than  $33^\circ$  elevation angles.

Table 2: Summary of the GPS CDF pseudorange bounding results for all analyzed data sets

Data set	Mean (cm)		Bounding standard deviation (cm)		Mean (cm)		Bounding standard deviation (cm)	
	L1				L2			
	702	1500	702	1500	702	1500	702	1500
No Truck	1.01	0.81	83	99	.84	3.08	96	112
EW Truck after exclusion	2.26	1.03	87	96	1.78	3.94	99	117
EW Truck Multipath	11.6	7.9	130	156	8.38	15.5	130	200
EW Truck Penetration	4.99	6.95	75	99	5.38	12.6	100	110
EW Truck >33 degree	3.27	1.54	48	58	0.98	4.31	43	58
EW Truck <33 degree	3.97	4.72	118	138	4.17	3.43	113	182
EW Truck Aggregate	2.18	1.34	113	132	2.12	3.96	107	174
NS Truck after exclusion	1.59	2.5	106	101	2.69	3.15	84	94
NS Truck Multipath	11.7	12.7	98	121	8.14	7.29	96	101
NS Truck Penetration	2.02	7.27	83	103	1.28	2.01	85	141
NS Truck >33 degree	2.32	3.89	53	62	1.84	1.38	49	67
NS Truck <33 degree	3.63	5.99	108	107	2.48	6.47	91	122
NS Truck Aggregate	1.15	1.81	104	103	2.13	2.94	87	117
<b>Maximum Values</b>	<b>11.7</b>	<b>12.7</b>	<b>130</b>	<b>156</b>	<b>8.38</b>	<b>15.5</b>	<b>130</b>	<b>200</b>

Table 3: Summary of the GLONASS CDF pseudorange bounding results

Data set	Mean (cm)		Bounding standard deviation (cm)		Mean (cm)		Bounding standard deviation (cm)	
	L1				L2			
	702	1500	702	1500	702	1500	702	1500
No Truck	1.02	1.08	185	113	0.83	1.95	82	101
EW Truck after exclusion	0.51	1.51	96.6	92.2	1.31	1.84	114	115
EW Truck Multipath	8.03	16	144	130	12.7	6.97	112	153
EW Truck Penetration	2.39	3.62	142	96.6	7.1	3.45	128	110
EW Truck >33 degree	1.07	2.6	41.9	59.3	1.11	1.67	48.4	62.2
EW Truck <33 degree	3.3	5.22	125	113	4.68	3.75	119	133
EW Truck Aggregate	1.07	1.15	119	108	2.2	1.88	112	126

NS Truck after exclusion	2.01	1.16	69.3	81.3	1.67	1.17	82.5	101
NS Truck Multipath	17	10.6	136	134	14.7	9.29	106	156
NS Truck Penetration	4.56	2.62	98.8	100	7.99	10.2	86.1	135
NS Truck >33 degree	1.17	2.49	45.5	46.5	0.85	2.28	48.5	69.3
NS Truck <33 degree	4.2	4.64	123	114	4.5	5.24	95.8	129
NS Truck Aggregate	1.02	1.11	118	108	1.7	1.77	92.1	123
<b>Maximum Values</b>	<b>17</b>	<b>16</b>	<b>185</b>	<b>134</b>	<b>14.7</b>	<b>10.2</b>	<b>128</b>	<b>156</b>

### B. Bounding standard deviation results – Carrier phase

In order to quantify the multipath effect on the carrier phase measurement, we compute the double difference carrier phase residuals. To isolate the source of the multipath error for a specific antenna, GNSS data was also collected at another antenna on a nearby building’s rooftop with open view to the sky. Also, only high elevation satellites above 33 deg elevation were used as reference satellites. The baseline vector between the tested antenna and the rooftop  $b_{12}$  was previously surveyed. Therefore, the carrier phase residual  $z_\phi$  can be computed as:

$$z_\phi = \Delta^2 \phi_{12} - \Delta e^T b_{12} - \lambda \left\lfloor \frac{\Delta^2 \phi_{12} - \Delta e^T b_{12}}{\lambda} \right\rfloor = \Delta v_{\phi_{12}} + \delta T + \delta I \quad (5)$$

where  $\Delta^2 \phi$  is the double difference carrier phase between two satellites and two antennas,  $\Delta e$  is the difference in line of sight vector from the antenna to both satellites, the operator  $\lfloor \cdot \rfloor$  was used to represent the nearest integer rounding operation, and the terms  $\delta T$  and  $\delta I$  represent residual differential ionospheric and tropospheric errors, which are negligibly small for the short baseline distance used in this test.

Figure 8 shows an example L1 double difference carrier phase residual for 702 antenna data in the No-Truck test scenario.

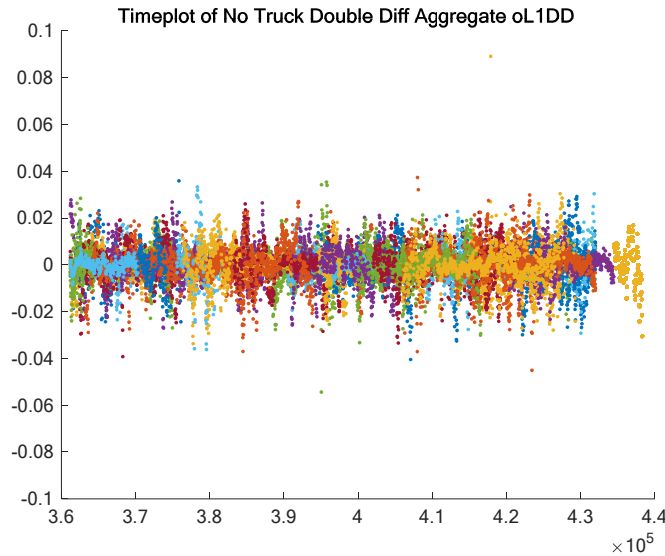


Figure 8: double difference carrier phase residual

The same bounding process that was applied to the pseudorange residual errors is also used for the E-W and N-S carrier phase data for all antennas and frequencies. A summary of results for both GPS and GLONASS data is shown in Tables 4 and 5, respectively. In general, the results suggest that penetration and MP regions have non-zero mean and that the bounding standard deviation in these regions is larger than under nominal clear-sky conditions. The results also show that L2 multipath errors are larger than for L1, but that the multipath standard deviations of the 1500 antenna and 702 antenna are relatively similar. The same analysis is repeated while distinguishing data at elevations lower than 33 degrees versus higher than 33 degrees. Low elevation satellite signals have more than 4 times larger bounding standard deviations than higher

elevation ones. For example, for the 702 antenna, the double difference GPS carrier phase error for high elevation satellites can be bounded by a Gaussian function with 0.92 mm mean and 8 mm standard deviation Gaussian distribution. The low elevation satellites, in contrast, need to be bounded considering 0.8 mm mean and 33mm standard deviation. These numbers are based on the maximum values corresponding to the L1 and L2 frequencies.

In some cases in Table 5, the mean of the double difference carrier phase error for GLONASS is lower than that of GPS because in GLONASS the float value of the ambiguity was subtracted from the residual in contrast to the integer value in GPS. Because GLONASS is a frequency division multiple access (FDMA) system, the double difference carrier phase residuals still contain inter-frequency biases that were not calibrated in this analysis.

Similar to the pseudorange case, if the largest bounding mean and standard deviation values are not causing the navigation system to violate availability requirements, then no more distinction is needed between regions of multipath, penetration, or clear sky. If, on the other hand, the requirements are not met with these bias and standard deviation values, then a more elaborate model is needed, where different error models are used based on elevation, for example, or where multipath and thermal noise are evaluated separately.

Table 4: Summary of the CDF GPS carrier phase bounding results for all analyzed data sets

Data set	Bounding standard deviation (mm)				Bounding standard deviation (mm)			
	Mean (mm)		Mean (mm)		Mean (mm)		Mean (mm)	
	L1	L2	L1	L2	L1	L2	L1	L2
	702	1500	702	1500	702	1500	702	1500
No Truck	0.30	.575	13.6	16.1	0.74	0.194	15.7	19.1
EW Truck after exclusion	0.36	0.39	12.4	26.8	0.22	0.46	14.4	17.9
EW Truck Multipath	1.05	0.91	12.3	14.5	0.53	1.69	18.8	18.1
EW Truck Penetration	0.81	0.32	21.9	27.1	3.42	2.44	25	29
EW Truck >33 degree	0.29	0.49	6.61	6.05	0.35	0.70	6.53	7.94
EW Truck <33 degree	0.25	0.40	19.1	27.4	0.57	0.51	21.2	25.9
EW Truck Aggregate	0.22	0.31	18.4	26.5	0.17	0.29	20.5	25.1
NS Truck after exclusion	0.18	0.11	16.8	18.2	0.50	0.30	19.4	24.2
NS Truck Multipath	0.34	0.30	13.6	14.4	1.05	0.17	23.9	23.3
NS Truck Penetration	0.76	0.99	33.3	19.8	1.82	1.31	12.8	19.1
NS Truck >33 degree	0.18	0.36	6.17	7.66	0.92	0.26	7.45	7.85
NS Truck <33 degree	0.49	0.34	29.9	18.5	0.75	0.40	21.3	24.7
NS Truck Aggregate	0.23	0.08	28.9	17.9	0.09	0.20	20.6	23.9
<b>Maximum Values</b>	<b>1.05</b>	<b>0.91</b>	<b>33.3</b>	<b>27.4</b>	<b>3.42</b>	<b>1.69</b>	<b>25</b>	<b>29</b>

Table 5: Summary of the CDF GLONASS carrier phase bounding results

Data set	Bounding standard deviation (mm)				Bounding standard deviation (mm)			
	Mean (mm)		Mean (mm)		Mean (mm)		Mean (mm)	
	L1	L2	L1	L2	L1	L2	L1	L2
	702	1500	702	1500	702	1500	702	1500
No Truck	0.13	0.133	11.2	15.6	0.23	0.32	12.2	18.3

EW Truck after exclusion	0.38	0.13	24.1	9.8	0.25	0.33	12.7	12.1
EW Truck Multipath	1.18	0.81	10.2	11.4	1.62	0.86	11.4	11.5
EW Truck Penetration	0.54	0.64	17	21.6	0.20	1.16	24	24.2
EW Truck >33 degree	0.42	0.27	6.5	4.91	0.38	0.26	5.8	5.96
EW Truck <33 degree	0.35	0.21	24.6	20.2	0.51	0.38	21.9	22.6
EW Truck Aggregate	0.30	0.15	23.6	19.5	0.19	0.18	21.1	21.9
NS Truck after exclusion	0.14	0.13	15.5	13.2	0.27	0.10	15.6	24.6
NS Truck Multipath	0.17	0.20	13.6	11.8	0.41	0.59	14.8	11.3
NS Truck Penetration	0.87	0.73	22.5	20.6	1.70	0.47	16	20.6
NS Truck >33 degree	0.28	0.30	6.7	7.81	0.76	0.47	7.3	7.85
NS Truck <33 degree	0.29	0.27	19.5	17.4	0.69	0.43	19.8	25.1
NS Truck Aggregate	0.15	0.08	18.9	16.8	0.08	0.09	15.5	24.3
<b>Maximum Values</b>	<b>1.18</b>	<b>0.81</b>	<b>24.6</b>	<b>21.6</b>	<b>1.70</b>	<b>1.16</b>	<b>24</b>	<b>25.1</b>

### C. Time constant results

Whenever the integrity risk of a Kalman filtering based positioning solution is required, it is critical to capture the colored noise temporal characteristics of the measurement noise. Multipath can be modeled as a first order Gauss Markov process, with a certain time constant. The goal of this analysis is to provide an experimental method to determine the value of the time constant. Figure 9 shows an example autocorrelation function for PRN3. It also shows a red horizontal line that corresponds to  $\exp(-1)$  value. The time at which the red line intersects the autocorrelation function is the first order Gauss Markov time constant that can be used in the Kalman filter.

A wide range of multipath correlation time constants was found when applying this process to all data sets. “Box plots” were used in Figure 10 to capture these results. The median value is indicated by a red horizontal line. The box shows the range of time constants containing 50% of all time constant values. The two small horizontal lines at the ends represent the limits where 99% of the time constant values lie. Red crosses represent all other values outside the 99% limits. The results for all GPS and GLONASS data sets are summarized in Tables 6 and 7, respectively. Time constant values are presented in terms of median, maximum, and 99% range values. Recent work in [3] describes a method to overbound the integrity risk given lower and upper bounds on the time constants of the colored noise’s autocorrelation function. The time constant computation is sensitive to the length of continuous tracking of the satellite. A new time constant is evaluated every time a loss of lock is detected or a reference satellite is switched. Time segments shorter than 600 seconds are not considered. Tables 6 and 7 show that the penetration case has shorter time constants than signals in the multipath region. The 1500 antenna has longer time constants than the 702 antenna. The penetration case exhibits lower time constants than the multipath case because it causes the signal to be weaker, which increases thermal noise levels. In contrast, reflected signals in multipath regions have almost the same signal strength as clear-sky signals, but multipath induces delays that change slowly based on antenna-to-reflector geometry.

In Tables 6 and 7, we also analyzed the time constant based on the satellite elevation angle. Data sets with elevation angles below 33 deg exhibit longer time constants because they are more likely to be affected by multipath (including ground multipath). High elevation satellites, in contrast, have in general shorter time constants. The same was concluded when analyzing the time constant of the carrier phase data (Tables 8 and 9).

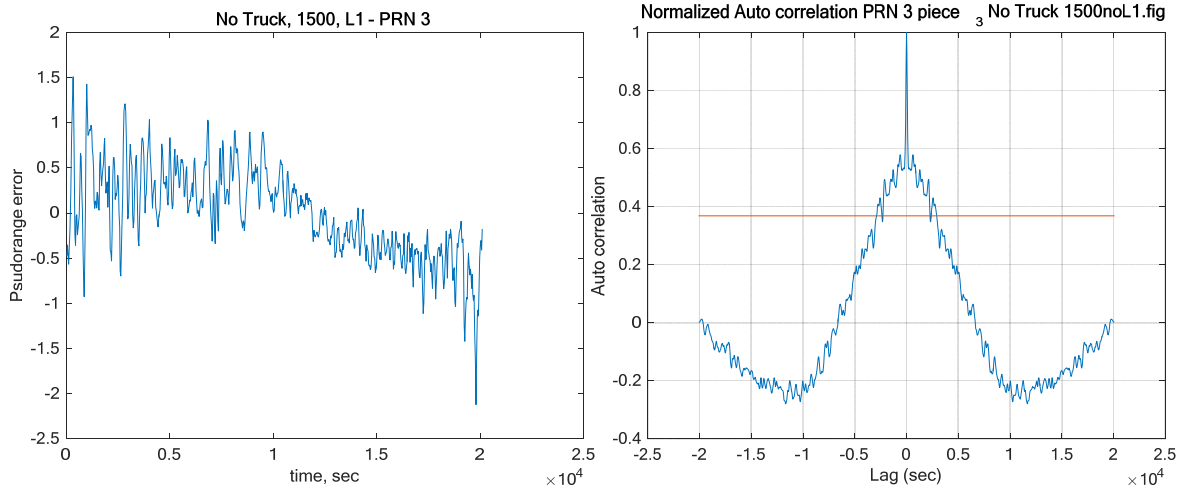


Figure 9: CMC error for PRN3 (left) and the corresponding autocorrelation time constant (right), with  $\exp(-1)$  line in red.

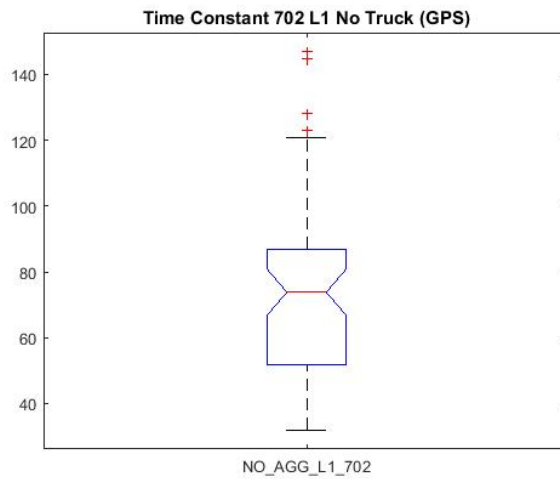


Figure 10: Autocorrelation time constant box plot for 702 antenna L1 frequency no-truck case data set

Table 6: summary of the time constant analysis for the GPS pseudorange phase

Data set	Median(sec)				99% of the data is in the range (sec)		Median (sec)		Max (sec)		99% of the data is in the range (sec)	
	702	1500	702	1500	702	1500	702	1500	702	1500	702	1500
	L1						L2					
No Truck	71	76	340	3116	32-121	28-137	63	64	229	3369	33-138	27-150
EW Direct	77	81	167	419	49-113	51-116	79	78	181	2038	42-143	31-180
EW Truck Multipath	107	98	137	148	86-146	87-177	120	107	184	211	73-208	96-224
EW Truck Penetration	64	64	103	114	41-107	44-84	74	68	150	226	38-130	54-112
EW Truck >33 degree	76	79	98	414	64-104	61-111	82	92	113	2005	63-129	50-174
EW Truck <33 degree	80	83	175	148	41-175	38-150	83	87	174	208	38-161	54-195
EW Truck Aggregate	77	86	142	143	41-143	38-145	85	91	130	192	38-164	55-217
NS Direct	85	83	1244	251	50-131	37-156	90	86	252	231	28-191	34-188

NS Truck Multipath	97	91	260	273	68-150	55-135	130	82	254	160	36-224	32-218
NS Truck Penetration	53	50	149	111	44-103	40-102	51	50	110	101	23-117	40-113
NS Truck >33 degree	87	82	428	125	81-118	56-126	106	99	151	237	77-158	60-182
NS Truck <33 degree	83	83	220	261	31-144	30-144	93	77	260	223	23-203	32-177
NS Truck Aggregate	84	88	220	220	36-139	30-144	97	80	189	223	25-221	32-187

Table 7: summary of the time constant analysis for the GLONASS pseudorange phase

Data set	Median(sec)		Max (sec)		99% of the data is in the range (sec)		Median (sec)		Max (sec)		99% of the data is in the range (sec)	
	702	1500	702	1500	702	1500	702	1500	702	1500	702	1500
	L1						L2					
No Truck	71	76	340	3116	41-101	26-122	63	64	229	3369	30-112	26-107
EW Direct	75	78	167	419	41-109	36-123	76	76	181	2038	44-109	43-136
EW Truck Multipath	107	95	137	148	78-137	75-123	117	106	184	211	81-159	83-196
EW Truck Penetration	64	64	103	114	40-83	41-77	74	68	150	226	43-95	42-124
EW Truck >33 degree	75	79	98	414	54-98	50-102	82	92	113	2005	60-95	42-126
EW Truck <33 degree	79	82	175	148	31-136	35-123	84	87	174	208	44-151	42-155
EW Truck Aggregate	77	86	142	143	40-134	35-138	84	91	130	192	45-130	42-150
NS Direct	85	83	1244	241	49-122	45-117	90	85	252	231	36-157	40-165
NS Truck Multipath	97	91	260	273	60-120	45-187	130	82	254	160	69-178	48-160
NS Truck Penetration	52	50	149	111	38-98	32-82	51	50	110	101	33-109	35-64
NS Truck >33 degree	87	82	428	125	59-116	46-115	106	99	151	237	48-151	47-147
NS Truck <33 degree	83	83	220	261	39-123	37-134	93	77	260	223	29-166	40-157
NS Truck Aggregate	84	87	220	220	43-126	39-131	97	79	189	223	29-166	40-153

Table 8: summary of the time constant analysis for the GPS carrier phase

Data set	Median(sec)		Max (sec)		99% of the data is in the range (sec)		Median (sec)		Max (sec)		99% of the data is in the range (sec)	
	702	1500	702	1500	702	1500	702	1500	702	1500	702	1500
	L1						L2					
No Truck	129	98	393	843	79-381	72-679	142	149	1563	1281	46-1403	45-1196
EW Direct	122	143	549	682	38-290	28-386	151	184	1588	765	28-534	47-410
EW Truck Multipath	155	149	283	433	67-214	90-236	146	148	220	235	114-175	108-215
EW Truck Penetration	105	59	485	134	21-300	19-134	102	57	448	315	26-212	15-165
EW Truck >33 degree	111	108	411	377	28-213	29-183	155	193	1588	584	48-531	65-337
EW Truck <33 degree	167	124	460	593	25-416	21-286	140	154	689	948	29-308	26-288
EW Truck Aggregate	170	130	460	593	37-392	21-273	149	165	1588	948	33-352	26-329
NS Direct	158	157	490	817	41-319	22-303	165	163	1565	1050	23-331	21-411
NS Truck Multipath	133	99	303	263	80-188	48-192	103	120	451	292	24-157	19-248
NS Truck Penetration	82	106	312	560	13-276	27-369	105	81	516	339	26-253	28-263
NS Truck >33 degree	129	150	271	962	56-254	52-446	165	203	1532	1142	59-1532	52-315
NS Truck <33 degree	142	157	426	584	13-305	22-314	124	115	556	460	23-322	21-270
NS Truck Aggregate	147	163	426	710	20-314	22-369	171	142	1565	541	23-331	21-341

Table 8: summary of the time constant analysis for the GLONASS carrier phase

Data set	Median(sec)		Max (sec)		99% of the data is in the range (sec)		Median (sec)		Max (sec)		99% of the data is in the range (sec)	
	L1	L2	L1	L2	L1	L2	L1	L2	L1	L2	L1	L2
	702	1500	702	1500	702	1500	702	1500	702	1500	702	1500
No Truck	126	112	376	320	25-314	18-256	159	150	839	388	25-357	21-280
EW Direct	116	86	372	519	31-184	18-202	133	123	794	631	14-447	26-268
EW Truck Multipath	115	99	229	154	7-175	55-154	110	119	188	184	81-157	64-172
EW Truck Penetration	49	63	489	516	16-97	22-210	71	70	553	503	18-194	27-167
EW Truck >33 degree	119	103	317	562	73-169	26-202	160	154	956	752	23-365	70-258
EW Truck <33 degree	101	96	533	519	23-308	22-200	114	82	605	545	14-365	27-195
EW Truck Aggregate	109	113	529	519	23-320	22-222	114	127	757	631	14-521	27-291
NS Direct	107	104	305	422	34-281	21-252	148	160	953	381	25-347	28-333
NS Truck Multipath	117	85	301	266	47-301	28-234	96	115	340	199	46-177	50-199
NS Truck Penetration	59	61	190	468	21-131	27-221	77	61	629	376	25-158	35-143
NS Truck >33 degree	116	122	483	1025	48-220	54-339	316	208	1134	986	88-1134	55-329
NS Truck <33 degree	108	91	305	314	36-234	34-251	106	114	245	430	25-245	29-259
NS Truck Aggregate	120	112	430	397	39-364	34-339	143	151	931	430	25-351	29-302

## DYNAMIC DATASET RESULTS

A dynamic test was conducted where an antenna was installed on top of a car and was driven for about 2 hours in different automotive operating environments. Throughout this test, signals reaching the antenna were subjected to obstructions typical of highway and downtown urban environments, including road signs, overpasses, high-rise buildings and urban canyons. The data was collected at 1Hz update rate and categorized in: Highway, Downtown-1, Downtown-2, and Residential areas.

For the dynamic test data set, it was not possible to distinguish multipath regions from penetration regions. Instead, data was sorted depending on the driving environment (highway, downtown, etc.), or low elevation versus high elevation. Furthermore, the carrier phase analysis was not conducted on the dynamic data set.

The same procedure of evaluating the pseudorange error for the static case was followed for the CMC dynamic case. In the dynamic case, time segments shorter than 30 seconds were ignored. A summary of GPS and GLONASS results is shown in Tables 9 and 10, respectively. The results suggest that for highway and typical residential environments, low elevation satellite signal tracking errors are bounded by Gaussian functions with mean and standard deviation at least twice that of the high elevation satellite signals. It is worth reminding that, in this study, the threshold for low versus high elevation is 33 degrees. For the urban canyon environment, however, high elevation satellites sometimes exhibit larger errors than low elevation ones. This can be due to several factors: 1- most low elevation satellites are being blocked and, therefore, high elevation sets have larger sample size, and 2- in the dynamic test, the environment was changing rapidly such that the source of multipath for low elevation satellites (billboards, traffic signs, or surrounding trucks) is not as persistent as for high elevation signals impacted by reflections off of tall buildings.

A time constant analysis similar to the one conducted for the static set was also performed on the dynamic data set. In the dynamic case, time segments shorter than 240 seconds were not considered. Tables 11 and 12 respectively provide GPS and GLONASS time constants, for all four test environments, for all satellites at low elevation and at high elevation. Because of how fast the environment is changing in the dynamic test, in general, the dynamic test data showed shorter time constants than the static test.

Table 9: Summary of the GPS CDF pseudorange bounding results for Dynamic data sets

Data set	Mean (cm)			Bounding standard deviation (cm)			Mean (cm)			Bounding standard deviation (cm)		
	L1						L2					
	Agg.	Low El	High El	Agg.	Low El	High El	Agg.	Low El	High El	Agg.	Low El	High El
No Truck	0.81	-	-	83.0	-	-	0.84	-	-	96.0	-	-
Downtown – 1	2.30	2.40	1.79	91.9	39.7	92.3	2.25	12.0	1.98	116	166	68.8
Downtown – 2	0.49	1.23	0.29	55.4	35.3	56.8	0.59	1.13	0.42	65.2	71.3	62.7
Highway	0.21	0.30	0.15	47.7	50.6	23.8	0.19	0.34	0.16	48.2	50.4	28.3
Residential	0.59	0.99	0.39	87.2	100	30.8	0.99	1.76	0.59	86.1	95.4	31.0
Maximum Values	2.30	2.40	1.79	91.9	100	92.3	2.25	12.0	1.98	116	166	68.8

Table 10: Summary of the GLONASS CDF pseudorange bounding results for Dynamic data sets

Data set	Mean (cm)			Bounding standard deviation (cm)			Mean (cm)			Bounding standard deviation (cm)		
	L1						L2					
	Agg.	Low El	High El	Agg.	Low El	High El	Agg.	Low El	High El	Agg.	Low El	High El
No Truck	1.02	-	-	113	-	-	0.83	-	-	82.0	-	-
Downtown – 1	1.85	3.35	1.72	112	87.9	114	1.20	1.71	1.77	132	86.7	134
Downtown – 2	0.93	1.98	1.32	220	241	106	0.65	1.14	1.10	168	70.8	173
Highway	0.49	0.79	0.20	60.3	62.7	27.5	0.40	0.77	0.25	52.1	54.8	28.3
Residential	0.76	1.16	0.69	112	124	22.7	0.49	1.72	0.40	108	126	37.7
Maximum Values	1.85	3.35	1.72	220	241	114	1.20	1.72	1.77	168	126	173

Table 11: Summary of the GPS time constant analysis

Data Sets		Median(sec)	Max (sec)	99% of the data is in the range (sec)	Median (sec)	Max (sec)	99% of the data is in the range (sec)
Highway	High El	28	44	13-44	18	29	5.8-20
	Low El	n/a	n/a	n/a	n/a	n/a	n/a
	Aggregate	28	44	13-44	13	29	6-20
Deerfoot	High El	27	123	9-64	22	157	5.6-51
	Low El	25	96	4.2-58	21	121	8.3-34
	Aggregate	27	123	4-64	22	157	5.6-60
Downtown	High El	25	158	2.5-69	18	154	3.6-53
	Low El	23	92	2.9-60	16	74	3-40

	Aggregate	24	158	2.6-66	16	154	3-44
Downtown Truth	High El	33	121	9-96	25	106	4.3-57
	Low El	32	56	10.7-56	23	55	6.9-55
	Aggregate	32	121	9-74	24	106	4.2-57

Table 12: Summary of the GLONASS time constant analysis

Data Sets		Median(sec)	Max (sec)	99% of the data is in the range (sec)	Median (sec)	Max (sec)	99% of the data is in the range (sec)
		L1			L2		
Highway	High El	18	32	2-23	16	27	1.8-27
	Low El	n/a	n/a	n/a	n/a	n/a	n/a
	Aggregate	18	32	2-23	16	27	1.8-27
Deerfoot	High El	24	71	9.7-53	21	74	1.8-48
	Low El	29	62	23-62	21	64	5.2-64
	Aggregate	26	71	9.7-63	21	98	1.8-48
Downtown	High El	19	116	1.8-55	19	152	2.4-67
	Low El	19	78	2.8-53	16	112	3.2-53
	Aggregate	18	116	1.8-55	17	152	2.4-57
Downtown Truth	High El	27	145	5-67	23	89	11-56
	Low El	32	98	6.9-42	25	71	10-45
	Aggregate	29	145	5-67	24	89	10-54

## CONCLUSION:

In this work, we proposed a methodology to quantify by post-processing GNSS pseudorange and carrier phase measurement errors encountered in automotive operating conditions. We first provided preliminary error models for code and carrier phase receiver noise and multipath under open-sky conditions and in the presence of a truck nearby a car-mounted GNSS antenna. These preliminary results showed that the truck induced about 60% increase in ranging measurement errors due to multipath. There were additional measurement errors associated with signals penetrating the truck's trailer, which caused about 20% increase in measurement error as compared to the open-sky case. Then, we carried out a correlation time constant analysis to show that the multipath error time constant is lower in the dynamic case (when the car is driving) than for the static case (when the car is not moving). In addition, this paper provides values for the multipath error's overbounding means and standard deviation, for both pseudorange and carrier phase signals. Results show that, when modeling multipath errors using overbounding Gaussian functions, a non-negligible mean must be accounted for to evaluate the integrity risk (or equivalently, protection levels).

Assuming that an automotive navigation system is not aware whether a received GNSS signal has penetrated or has been reflected off of a surrounding object (like a truck trailer), we can summarize overbounding standard deviation for pseudorange receiver noise and multipath errors as shown in Tables 13-14. Two modeling approaches are considered: one that distinguished low versus high elevation satellites in Table 13, and the other than uses the overall maximum value of the bounding sigma in Table 14. The same was done for carrier phase receiver noise and multipath errors in Tables 15-16.

Table 13: Summary of the CDF pseudorange bounding results for low and high elevation satellites

		GPS		GLONASS	
		Mean (cm)	sig (cm)	Mean (cm)	sig (cm)
L1	Low El	12.7	156	17	241
	High El	3.89	92.3	2.6	114
L2	Low El	15.5	200	14.7	168
	High El	4.31	68.8	2.28	173

Table 14: Summary of the maximum CDF pseudorange bounding results

	GPS		GLONASS	
	Mean (cm)	sig (cm)	Mean (cm)	sig (cm)
L1	12.7	156	17.0	241
L2	15.5	200	14.7	173

Table 15: Summary of the CDF carrier phase bounding results for low and high elevation satellites

		GPS		GLONASS	
		Mean (cm)	sig (cm)	Mean (cm)	sig (cm)
L1	Low El	0.05	3.00	0.04	2.46
	High El	0.05	0.76	0.04	0.78
L2	Low El	0.08	2.59	0.07	2.51
	High El	0.10	0.79	0.08	0.79

Table 16: summary of the maximum CDF carrier phase bounding results

	GPS		GLONASS	
	Mean (cm)	sig (cm)	Mean (cm)	sig (cm)
L1	0.10	3.33	0.12	2.46
L2	0.34	2.90	0.17	2.51

Error model refinement can be achieved considering higher- rate data in the static test, which will facilitate the distinction between thermal noise and slow multipath errors. This paper only captures typical automotive conditions. Anomalous conditions including excessive multipath will have to be analyzed separately to ensure navigation system integrity.

## ACKNOWLEDGEMENTS

The authors would like to thank the NovAtel, part of Hexagon Positioning Intelligence, for their continued support of this research effort. The opinions in this paper are our own and do not represent those of any other person or organization. The authors would also like to thanks Austin Gonzalez and Anas Darwich for their assistance in processing the experimental data sets.

## REFERENCES

- [1] B. DeCleene, "Defining Pseudorange Integrity - Overbounding," *Proceedings of the 13th International Technical Meeting of the Satellite Division of The Institute of Navigation (ION GPS 2000)*, Salt Lake City, UT, September 2000, pp. 1916-1924.
- [2] J. Rife, S. Pullen, P. Enge, and B. Pervan, "Paired Overbounding for Nonideal LAAS and WAAS Error Distributions," *IEEE Transactions on Aerospace and Electronic Systems*, Vol. 42, No. 4, October 2006, pp. 1386-1395.

- [3] Langel, Steven E., Joerger, Mathieu, Khanafseh, Samer M., Pervan, Boris S., "A New Look at Bounding Integrity Risk in the Presence of Time-Correlated Errors," *Proceedings of the 30th International Technical Meeting of The Satellite Division of the Institute of Navigation (ION GNSS+ 2017)*, Portland, Oregon, September 2017, pp. 2436-2451.
- [4] P. Misra and P. Enge, *Global Positioning System signals, Measurements, and Performance*. Lincoln, MA: Ganga-Jamuna Press, 2001.
- [5] T. Murphy, R. Snow, M. Braasch, "GPS Multipath on Large Commercial Air Transport Airframes", *NAVIGATION, Journal of The Institute of Navigation*, Vol. 43, No. 4, Winter 1996-1997, pp. 397-406.
- [6] D. Akos, J. Weiss, T. Murphy, S. Pullen, "Airborne Multipath Investigation via a GPS Software Receiver," *Proceedings of the 17th International Technical Meeting of the Satellite Division of The Institute of Navigation (ION GNSS 2004)*, Long Beach, CA, September 2004, pp. 1822-1831.
- [7] Murphy, Tim, Harris, Matt, Geren, Preston, Pankaskie, Tom, Clark, Barbara, Burns, Jason, "More Results from the Investigation of Airborne Multipath Errors," *Proceedings of the 18th International Technical Meeting of the Satellite Division of The Institute of Navigation (ION GNSS 2005)*, Long Beach, CA, September 2005, pp. 2670-2687.
- [8] W. Preston Geren, T. Murphy, T. A. Pankaskie, "Analysis of Airborne GPS Multipath Effects using High-Fidelity EM Models," *IEEE Trans. on Aerospace and Electronic Systems*, Vol. 44, No. 2, April 2008
- [9] Y. S. Park "Design of Airport Surface Movement Using Single-Frequency GPS," Ph.D. Dissertation, Stanford University, 2016.
- [10] S. Zhang, S. Lo, Y.H. Chen, T. Walter, P. Enge, "GNSS Multipath Detection in Urban Environment Using 3D Building Model," *Proceedings of IEEE/ION PLANS 2018*, Monterey, CA, April 2018, pp. 1053-1058.
- [11] Federal Highway Administration, "Vehicle positioning trade study for ITS applications (Report No. FHWA-JPO-12-064)," April 2012